Effect of confinement on the solid-liquid coexistence of Lennard-Jones Fluid

Cite as: J. Chem. Phys. **139**, 174706 (2013); https://doi.org/10.1063/1.4827397
Submitted: 31 July 2013 . Accepted: 15 October 2013 . Published Online: 06 November 2013

Chandan K. Das, and Jayant K. Singh

Effect of confinement on the solid-liquid coexistence of Lennard-Jones Fluid

Chandan K. Das and Jayant K. Singh[a)]
Department of Chemical Engineering, Indian Institute of Technology Kanpur, Kanpur 208016, India

(Received 31 July 2013; accepted 15 October 2013; published online 6 November 2013)

The solid-liquid coexistence of a Lennard-Jones fluid confined in slit pores of variable pore size, H, is studied using molecular dynamics simulations. Three-stage pseudo-supercritical transformation path of Grochola [J. Chem. Phys. **120**(5), 2122 (2004)] and multiple histogram reweighting are employed for the confined system, for various pore sizes ranging from 20 to 5 molecular diameters, to compute the solid-liquid coexistence. The Gibbs free energy difference is evaluated using thermodynamic integration method by connecting solid-liquid phases under confinement via one or more intermediate states without any first order phase transition among them. Thermodynamic melting temperature is found to oscillate with wall separation, which is in agreement with the behavior seen for kinetic melting temperature evaluated in an earlier study. However, thermodynamic melting temperature for almost all wall separations is higher than the bulk case, which is contrary to the behavior seen for the kinetic melting temperature. The oscillation founds to decay at around $H = 12$, and beyond that pore size dependency of the shift in melting point is well represented by the Gibbs-Thompson equation.
 [http://dx.doi.org/10.1063/1.4827397]

I. INTRODUCTION

Melting, the phenomenon of phase transition from a crystalline solid state to a liquid state is the most common structural transition and plays an important role in materials science and engineering,[1] nature such as in frost heaving, and biology. In recent years, a greater attention has been given to studying melting/freezing phenomena of confined fluids in relevance to various fields of modern technology such as micro-fluidics, fabrication of nanomaterials, adhesion, nanotribology, and nanotechnology.[2]

Several experimental studies have been reported on melting and freezing in well-characterized porous materials.[3–5] The melting temperature of the confined solid also depends on the relative strength of the wall-fluid interaction and the hysteresis associated with the phase transition.[6,7] Decrease in the freezing temperature is observed for oxygen in sol–gel glasses of pore size distribution 2.2–18.7 nm.[8] The freezing and melting temperatures of indium are less compared to the bulk value and vary inversely with pore diameter in porous silica glasses.[4] In contrast to these results for glasses, some other experiments have reported a significant increase in the melting temperature.[5] In the case of colloidal suspension, confined in a channel, reducing the channel size changes the system behavior from three-dimensional (3D) to two-dimensional (2D), and colloidal monolayer displays continuous 2D melting.[9–12]

Numerous molecular simulation techniques have been implemented to understand the freezing and melting behavior of confined molecular systems.[6,13,14] The demonstration of the freezing transition and phase diagrams of hard sphere confined in hard slit and cylindrical pores have been reported using molecular simulations[15] and free-volume theory.[16] The elevation/depression of the freezing point is found to depend on the relative strength of the wall–fluid interaction, and the width of the hysteresis also depends on the nature of the surfaces.[17] Depression of the freezing point is also observed in weakly attractive cylindrical pores of diameter 1.5–3.5 nm.[18] The freezing temperature strongly depends on the fluid-wall interaction strength as observed by few workers.[17–23] Evidence of transition from a 2D liquid phase to a hexatic phase is observed for simple fluids in narrow slit pores.[24] In case of mixtures, both an elevation and a depression in the freezing temperature are observed, depending on the mole fractions of the components.[25] The freezing/melting behaviors of confined fluids have been related to variations in the ratio of wall–fluid and fluid–fluid interactions.[21,23]

Different molecular simulation methods exist for the determination of the melting/freezing temperature. In case of bulk solid, heuristic methods based on Lindemann parameter,[26,27] Born criteria (bulk),[28] non-Gaussian parameter[26] have been used successfully. In other cases, structural parameters, such as static order parameter,[29] structure factor,[17,30–33] radial distribution function, and orientational correlation function,[18,22] are commonly used to estimate the melting/freezing temperature. However, true melting/freezing temperature or thermodynamic melting temperature requires calculation of free-energy difference which can be evaluated using thermodynamic integration[18,23,34] for simple systems. Other methods which have also been used to evaluate the thermodynamic melting temperature are phase-switch method[35] and self-referential method.[36–40]

In case of confined solids, structural parameters are commonly used to evaluate melting temperature.[17] Dominguez and co-workers[14] have evaluated the phase diagram of

a)Author to whom correspondence should be addressed. Electronic mail: jayantks@iitk.ac.in

confined Lennard-Jones fluids for weakly and repulsive pores, using thermodynamic integration method. In particularly, Einstein crystal was used as a reference for the determination of Gibbs free energy of the solid phase. Radhakrishnan *et al.*[21] have used the Landau theory to calculate the free energy as a function of bond orientation order parameter, using umbrella sampling method, to estimate the melting temperature. Wan *et al.*[41] have used free energy method based on Einstein crystal reference to compute fluid-solid transition under confinement. In our recent work, we have extended the Lindemann and non-Gaussian parameters to estimate the melting temperature for confined Lennard Jones solids, which was well supported by structural and bond orientational order parameters.[20] However, melting temperature estimate is tricky from non-Gaussian parameter due to the presence of multiple peaks, of similar intensity, in close proximity to the melting transition. Further, heuristic methods yield kinetic melting temperature, which is not yet compared with the thermodynamical melting temperature of confined solids.

Earlier studies[5,8,17,24,34,42] on confined solid in slit pore showed that elevation and depression of melting/freezing temperatures are more or less linearly related to the inverse of the slit separation. Mostly their attentions were limited to freezing transition on quenching the system. Moreover, the basic measurements behind most of the earlier studies were positional/orientational correlation function. However, recent work of Kaneko *et al.*[42] reports an oscillatory behavior of melting and freezing temperatures with pore size. The results based on discontinuity in potential energy and density with temperature were in good agreement with that using the Clausius–Clapeyron equation for the slit system.[43] Wan *et al.*,[41] on the other hand, showed an oscillatory nature of the free energy of the confined solid with pore size. Oscillatory nature of the melting temperature is also observed in our earlier work using heuristic methods.[20] These recent results raise a doubt on the earlier believed linear nature of the melting/freezing temperature with inverse of the pore size. Motivated from the aforementioned works, our goal in this study is to provide more clarity in the nature of melting behavior of confined solids from a thermodynamic approach and compare the prediction via heuristic methods. In this work, we have extended the pseudo-supercritical transformation path method of Grochola's[44] along with multiple histogram reweighting (MHR) method for precise determination of the melting temperature of confined Lennard-Jones (LJ) systems. The pseudo-supercritical transformation path method is based on the thermodynamic integration approach, which is distinct from the methods adopted by earlier workers.[14,21,41] The estimate of order-disorder transition temperature of confined solid by Wan *et al.*[41] was based on visual inspection and 2D order parameter calculations. On the other hand, Kaneko *et al.*[42] have estimated the freezing/melting temperature from the discontinuities in the potential energy and density; hence solid-liquid coexistence temperature under confinement was not investigated. The method of Radhakrishnan *et al.*[21] based on Landau theory determines the free energy as a function of order parameter. However, it requires efficient sampling of liquid and solid phases, which is difficult to achieve without incorporation of advanced algorithms. Dominguez and co-workers,[14] on the other hand, evaluated the free energy for the liquid and solid phases independently in order to find a coexistence point under confinement. The method adopted here is similar in principle but avoids direct calculation of free energy of liquid and solid phases. Instead, free energy difference is evaluated by means of thermodynamic integration and multiple histogram reweighing methods. Hence, the current method overcomes the hurdle faced by Dominguez and co-worker and is more efficient because of multiple histogram reweighting technique. We first present the details of the free energy method for evaluating the solid-liquid coexistence under confinement. Subsequently, we evaluate melting temperature of a LJ solid for slit pore size ranging from 8 to 5 molecular diameters, and compared with the corresponding kinetic melting temperature. Further, we estimate thermodynamic melting temperature of the LJ solid for larger pore sizes, from 12 to 20 molecular diameters. The rest of the paper is organized as follows. The model and method are described in Sec. II. In Sec. III, some details of the simulations are provided, and in Sec. IV, the results are presented and discussed. Finally, concluding remarks are presented in Sec. V.

II. MODEL AND METHODS

A. Potential models

For fluid–fluid interactions, the truncated and shifted LJ potential is used in the following form:

$$U_{ff}^{tr-sh} = \begin{cases} U_{ff}^{lj}(r) - U_{ff}^{lj}(r_c) & r \le \mathrm{r}_c \\ 0 & r > \mathrm{r}_c \end{cases}, \qquad (1)$$

where

$$U_{ff}^{lj}(r) = 4\varepsilon_{ff}\left[\left(\frac{\sigma_{ff}}{r}\right)^{12} - \left(\frac{\sigma_{ff}}{r}\right)^{6}\right],$$

where σ_{ff} is the particle diameter, ε_{ff} is the interaction well depth, and r is the distance between two particles. All quantities are reduced with respect to ε_{ff} and σ_{ff}. Cut-off radius, $r_{c,}$ is fixed at $5\sigma_{ff}$.

In this work, the pore is modeled as a slit pore with structure-less walls. Interaction between the wall and a fluid particle at is distance z is defined by LJ 9-3 potential.[7] The potential form is as follows:

$$U_{wf}(z) = \frac{2}{3}\pi\rho_w\varepsilon_{wf}\sigma_{wf}^3\left[\frac{2}{15}\left(\frac{\sigma_{wf}}{z}\right)^9 - \left(\frac{\sigma_{wf}}{z}\right)^3\right], \qquad (2)$$

where ρ_{w} is the number density of atoms in the wall, the subscripts f and w represent fluid and wall, respectively. σ_{wf} and ε_{wf} are the cross parameters for the wall-fluid interaction. In this work, we fix $\sigma_{ff} = 1$, $\varepsilon_{ff} = 1$, $\sigma_{ww} = 0.8924$, $\varepsilon_{ww} = 0.1891$, $\rho_w = 6.3049$, $\sigma_{wf} = (\sigma_{ff} + \sigma_{ww})/2$, and $\varepsilon_{wf} = (\varepsilon_{ff}\,\varepsilon_{ww})^{0.5}$, as per Refs. 7 and 20. The strength of interaction of the wall-fluid relative to fluid-fluid interaction is define by the coefficient, $\alpha = \rho_{\mathrm{w}}\varepsilon_{\mathrm{wf}}\sigma^3{}_{\mathrm{wf}}/\varepsilon_{\mathrm{ff}}$, which is fixed at 2.32. LJ 9-3 pore size is varied from 5 to 20 molecular diameters. In this work, all quantities are reduced with respect to σ_{ff} and ε_{ff}.

In addition to LJ 9-3 wall, Steele 10-4-3 potential[45] is also used for the wall-fluid interaction. The detail of the potential form is given below:

$$\phi_{fw}(z) = 2\pi\rho_w\varepsilon_{fw}\sigma_{fw}^2\Delta\left[\frac{2}{5}\left(\frac{\sigma_{fw}}{z}\right)^{10} - \left(\frac{\sigma_{fw}}{z}\right)^4 - \left(\frac{\sigma_{fw}^4}{3\Delta(z+0.61\Delta)^3}\right)\right], \quad (3)$$

where Δ the separation between two consecutive planes of graphite is 0.879, z is the distance of a particle from the wall. The strength of interaction of the wall-fluid relative to fluid-fluid interaction is defined by $\alpha = \rho_w\varepsilon_{wf}\sigma^2{}_{wf}\Delta/\varepsilon_{ff}$. For this case, H is fixed to 7.5. Two different values of relative wall-fluid interaction are chosen: $\alpha = 1.64$ and 2.14, to compare our results with the work of Radhakrishnan and co-workers.[21]

For a particular pore width, H, the total potential energy is given by

$$\phi_{pore} = \sum_{i=1}^{N}[\phi_{fw}(z_i) + \phi_{fw}(H - z_i)], \quad (4)$$

z_i is the distance of a molecule perpendicular to a pore wall and H is the distance between the two pore walls and N is the number of particles.

B. Simulation methodologies

There are many thermodynamic routes for evaluating the true freezing/melting temperature. More details of this aspect have been summarized by Monson and Kofke.[46] Generally three types of methods are available to determine the melting curve of a material in molecular dynamics, one-phase, or heat-until-it melts (HUM) method,[26] two-phase or solid-liquid coexistence (TP) method,[47] and the free energy method.[30] In this work, we adopt a different route, based on the free energy analysis, to determine the solid-liquid coexistence under confinement. Free energy analysis is one of the powerful techniques to predict the phase transition point. The estimation of melting temperature from free energy analysis consists of four steps: (a) the estimation of approximate melting point from density-temperature hysteresis curve; (b) the computation of equation of state for the solid and liquid phases using multiple histogram reweighting method at a reference state point; (c) the determination of difference in free energy between solid and liquid phases at an approximate melting temperature using the pseudo-supercritical transformation path; and (d) finally using the steps (b) and (c) evaluating the temperature where Gibbs free energy is zero, which is consider as the melting temperature. Each step is described below in detail.

1. Estimation of an approximate melting point

The method used for computing an apparent melting point is as follows. First we progressively heat and quench solid and liquid phases, respectively, using an isothermal-isobaric ensemble ($NP_{xx}(=P_{yy})HT$) at $P_{xx} = P_{yy} = 1.0$. As the liquid is quenched, the density gradually increases and at a certain temperature the density rises sharply. In case of the heating cycle, the density decreases and at a particular temperature the density drops sharply. We locate an approximate melting point within the hysteresis loop at which an abrupt change in density occurs.

2. Solid and liquid equation of state

The second step is the generation of the Gibbs free energy as a function of temperature for the solid and liquid phases with respect to their respective reference state points. This is done using the multiple histogram reweighting (MHR) technique of Ferrenberg and Swendsen.[48,49] Sandler and co-workers[50,51] used this technique in their reference state melting point simulations. MHR technique has been used successfully for the estimation of solid-liquid coexistence point.[52] Although the MHR technique has been elucidated in Refs. 48–51, 53, and 54, for completeness we provide a brief summary of its implementation in this study.

The Gibbs free energy $G(N,P,T)$ can be connected to the isothermal-isobaric partition function $\Delta(N,P,T)$ by the following relationship:

$$G(N, P, T) = -k_B T \ln \Delta(N, P, T), \quad (5)$$

where

$$\Delta(N, P, T) = \frac{1}{V_0\Lambda^{3N}N!}\iint \exp^{-\beta[U(r^N)+PV]}\, dr^N dV, \quad (6)$$

$$= \frac{1}{\Lambda^{3N}N!}Z(N, P, T), \quad (7)$$

where $\Lambda = h/\sqrt{2\pi m k_B T}$ is the thermal de Broglie wavelength and $Z(N,P,T)$ is the configurational contribution to the isothermal-isobaric partition function. $\mathbf{r}^N$ indicates the position vectors for all particles, and $U(\mathbf{r}^N)$ is the total potential energy of the system which is a sum of fluid-fluid interaction(U_1) and wall-fluid interaction(U_2). V_0 is the reference volume. The probability distribution function of finding a system with a potential energy $U(U = U_1 + U_2)$ and volume V for the NPT ensemble is

$$\wp(U, V; N, P, T) = \frac{\Omega(N, V, U)\exp(-\beta U - \beta PV)}{Z(N, P, T)}, \quad (8)$$

where $\Omega(N, V, U)$ is the microcanonical partition function. By collecting a two-dimensional histogram $H(U,V)$ of the frequency in which the system is observed with a potential energy U and volume V during a NPT ensemble simulation, the probability can be determined by

$$\wp(U, V; N, P, T) = \frac{H(U, V)}{\kappa}, \quad (9)$$

where $\kappa = \sum_{U,V} H(U, V)$. By equating Eqs. (8) and (9) and rearranging, the following expression is obtained:

$$\Omega(N, V, U) = \frac{H(U, V)Z(N, P, T)}{\kappa\exp(-\beta U - \beta PV)}. \quad (10)$$

The microcanonical partition function can be evaluated in the region where the histogram $H(U,V)$ is nonzero. The microcanonical partition function for the ith run can be transferred as a local approximation of the global partition function. Histograms from m runs can therefore be combined to generate a global thermodynamic landscape of the system. This can be done, using a weighting function $p_i(N, V, U)$, proposed by Ferrenberg and Swendsen,[49] which is used to combine histograms from several simulations according to

$$\Omega(N, V, U) = \sum_{i=1}^{m} \Omega_i(N, V, U)\, p_i(N, V, U). \tag{11}$$

The form of weighting function is

$$p_i(N, V, U) = \frac{\kappa \exp(-\beta_i U - \beta_i P_i V) / Z(N, P_i, T_i)}{\sum_{j=1}^{m} \kappa \exp(-\beta_j U - \beta_j P_j V) / Z(N, P_j, T_j)}. \tag{12}$$

Combining the multiple histograms to create a global approximation of $\Omega(N, V, U)$, the probability expressed by Eqs. (8) and (9) can be more accurately presented as

$$\wp(U, V; N, P_i, T_i) \frac{\sum_{j=1}^{R} H_j(U, V) \exp(-\beta_i U - \beta_i P_i V)}{\sum_{m=1}^{R} \kappa_m \exp(-\beta_m U - \beta_m P_m V) Z_i / Z_m}, \tag{13}$$

where R is the total number of histograms collected and $Z_i = Z(N, P_i, T_i)$. Equation (13) uses the fact that absolute value of partition function is not feasible; however, it is easy to find out the ratios of the partition functions. It is necessary to construct a normalized probability distribution, since our interest is to construct free energy curves considering a single state point as a reference state in such a way that the histograms overlap. The form of normalized probability distribution function is

$$\wp'(U, V; N, P_i, T_i) = \frac{\sum_{j=1}^{R} H_j(U, V) \exp(-\beta_i U - \beta_i P_i V)}{\sum_{m=1}^{R} \kappa_m \exp(-\beta_m U - \beta_m P_m V - c_m)}, \tag{14}$$

where

$$\exp(C_i) = \frac{Z(N, P_i, T_i)}{Z(N, P_1, T_1)} = \sum_{V} \sum_{U} \wp'(U, V; N, P_i, T_i). \tag{15}$$

By defining the ''weights'' C_i in this way, all partition function values for simulations $i = 2 \ldots R$ are determined with respect to the value at $i = 1$. With the help of a good initial guess values for the weights Eq. (14) can be solved easily and then iterating between Eqs. (14) and (15) until convergence, accurate values of the partition function relative to a fixed state point can be determined. Using the converged values of the weights, the normalized probability distribution can be presented by the relationship

$$\wp(U, V; N, P, T) = \wp'(U, V; N, P, T) \exp\left(-C_i^z\right). \tag{16}$$

The weights will be defined as

$$C_i^Z = \ln \frac{Z(N, P_i, T_i)}{Z(N, P_1, T_1)}. \tag{17}$$

The superscript z in the weights represent that they have been determined using configurational partition function. Finally combining Eqs. (5)–(7) with the definitions of the weights, it is possible to relate the two different types of weights to total free energy difference relative to a reference as follows:

$$C_i = C_i^Z + \frac{3N}{2} \ln \frac{T_i}{T_1} = \beta_1 G_1 - \beta_i G_i, \tag{18}$$

where $G_i = G(N, P_i, T_i)$. From this it can be seen that the multiple histogram reweighting method yields values of free energy for multiple state points relative to one fixed state point. The phase coexistence point can be determined with the help of histogram reweighting method itself as shown effectively by Eike *et al.*[52] For this purpose, it requires collection of histograms which can sample both regions of phase space for the two phases. However, for the case of solid-liquid coexistence, only multiple histogram reweighting method is not sufficient due to the free energy barrier between the two phases makes it difficult for a single simulation to adequately sample both solid and liquid regions of phase space, without use of smarter methods such as phase switch Monte Carlo technique. In this work, we perform two separate set of simulations for the liquid and solid phase. Free energy curves for liquid and solid phases are constructed from histograms, with different reference state points. Note that in the above equations P is $P_{xx} = P_{yy}$ and $V = AH$, where A is the area of the slit wall and H is the pore size.

3. Determination of solid-liquid free energy difference at the approximate melting temperature

The Helmholtz free energy difference between the solid and liquid phases at an approximate melting temperature is computed, according to a modified form of the three-stage pseudo-supercritical thermodynamic transformation path which is originally proposed by Grochola.[44] The transformation method is developed, based on the construction of a reversible thermodynamic path between the solid and liquid phases through one or more intermediate states. The necessary and sufficient condition of the intermediate states is that there must not be any presence of phase transition between them and the solid and liquid phases. The free energy along this pseudo-supercritical path is computed with a standard thermodynamic integration procedure. The fundamental equation for thermodynamic integration is

$$\Delta A^{ex} = \int \left\langle \frac{dU}{d\lambda} \right\rangle_{NVT\lambda} d\lambda, \tag{19}$$

where A^{ex} is the difference in excess Helmholtz free energy, λ is the integration path variable which is also known as Kirkwood's coupling parameter. Typically λ vary from zero to 1 such that when $\lambda = 0$ system act as reference state and $\left\langle \frac{dU}{d\lambda} \right\rangle_{NVT\lambda}$ indicates the NVT ensemble average for a particular value of λ. The Helmholtz free energy can be transferred to the Gibbs free energy by the addition of pressure-volume

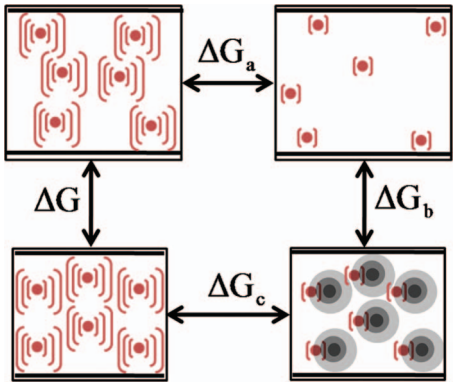

FIG. 1. The schematic representation of the three-step pseudo-supercritical transformation path for the confined system. (a) The liquid phase is converted to a weakly interacting fluid by gradually reducing the intermolecular interactions. (b) Gaussian potential wells are turned on while the volume is reduced to produce a weakly interacting ordered phase. (c) Gaussian wells are turned off while simultaneously intermolecular interactions are gradually restored to achieve a crystalline phase.

energy from the change in volume throughout the three-stage path. The pseudo-supercritical transformation pathway is as follows. In stage a, a fully interacting liquid phase is reduced from full intermolecular interactions to weak intermolecular interactions. In stage b, weakly attractive fluid phase is converted into solid constrained fluid phase using Gaussian wells. In the final stage c, the Gaussian wells are turned off while the full intermolecular interactions are brought back. Below, the formulation of the potential energy as a function of λ along with the derivative required for integration is described for each stage. The schematic diagram of three-stage pseudo-supercritical transformation path is presented in Fig. 1.

a. Stage a The goal of first step of the pseudo-supercritical path is the conversion of the fully interacting liquid to a weakly interacting fluid. This is accomplished through a coupling parameter λ, which scales intermolecular interactions in the following manner:

$$U_a(\lambda) = [1 - \lambda(1-\eta)]\, U_{inter}(r^N) + \phi_{fw}, \tag{20}$$

where $U_{inter}(\mathbf{r}^N)$ is the intermolecular potential energy based on the positions of all N particles, ϕ_{fw} represents potential energy due to wall-fluid interaction, independent of coupling parameter, and η is a scaling parameter such that: $0 < \eta < 1$. The derivative of this function gives

$$\frac{\partial U_a}{\partial \lambda} = -(1-\eta)\, U_{inter}(r^N). \tag{21}$$

b. Stage b In the second stage, simulation box volume is decreased from the liquid volume to the solid volume. To bring back the liquid particles to the lattice points corresponding to the solid phase, Gaussian attractive potential wells are introduced, situated at the lattice points of the crystalline phase. Box dimensions along the non-confined dimensions (L_x, L_y) of liquid and solid (i.e., box volume) phases must be known at the apparent melting temperature, either from the MHR results or from isothermal-isobaric simulation runs. This ensures that the liquid and solid phase pressures ($P_{xx} = P_{yy}$) are equal at the beginning of stage-a and at the end of the transformation path. The potential energy based on λ for this stage is

$$U_b(\lambda) = \eta U_{inter}[r^N(\lambda)] + \lambda U_{Gauss}\left[r^N(\lambda), r^N_{well}(\lambda)\right] + \phi_{fw}, \tag{22}$$

where $\mathbf{r}^N(\lambda)$ and $\mathbf{r}_{well}{}^N(\lambda)$ are the Cartesian coordinates of the particles and potential wells, respectively, which is function of λ due to the changing box volume. To relate Cartesian position change to box volume change, the identity $\mathbf{r} = \mathbf{Hs}$ is used to convert the Cartesian vector $\mathbf{r}$ to the fractional coordinate vector $\mathbf{s}$ using the cell basis matrix $\mathbf{H}$:

$$\mathrm{H}(\lambda) = \mathrm{H}_l - \lambda(\mathrm{H}_l - \mathrm{H}_s), \tag{23}$$

where the subscripts l and s indicate the cell basis matrix for the liquid and solid phases, respectively. As the system is confined in the z dimension only x and y dimensions are free to change. The Gaussian potential is given as

$$U_{Gauss}\left[r^N(\lambda), r^N_{well}(\lambda)\right] = -\sum_{i=1}^{N}\sum_{k=1}^{N_{wells}} \lambda a_{ik} \exp\left[-b_{ik} r^2_{ik}(\lambda)\right], \tag{24}$$

where N_{wells} is the number of Gaussian potential wells situated at lattice point of N particles, a_{ik} and b_{ik} are the parameters describing how particle i interacts with potential well k, and $r^2_{ik}(\lambda) = |r_i(\lambda) - r_{well,k}(\lambda)|^2$represents the distance between atom i and well k. In this work, $N_{wells} = N$. The value of parameters a and b is taken according to Grochola.[44] The value of parameter "b" is chosen such a way that $U_{Gauss}[r^N(\lambda), r^N_{well}(\lambda)] \approx 1 \times 10^{-5}\varepsilon_{ff}$ at a distance of $1.4\sigma_{ff}$, on the other hand amplitude constant, "a" is equivalent to $8.0\varepsilon_{\mathrm{ff}}$.

The derivative of U_b with respect to λ is evaluated using the relationship for the pressure tensor,[55] which is

$$-\frac{\partial U_{inter}}{\partial H_{\alpha\gamma}} = \sum_{\beta} \mathrm{P}^{ex}_{\alpha\beta} V \mathrm{H}^{-1}_{\gamma\beta}. \tag{25}$$

Using the above relation, and considering that the current system is confined in the z direction, and for isotropic changes only in the x and y directions, the derivative of the potential function is given by

$$\frac{\partial U_b}{\partial \lambda} = \sum_{\beta=x,y} V(\lambda)\, H^{-1}_{\beta\beta}(\lambda) \Delta H_{\beta\beta} \left(\eta \mathrm{P}^{ex}_{\beta\beta} + \lambda \mathrm{P}^{ex}_{Gauss,\beta\beta}\right) + \mathrm{U}_{Gauss}\left[r^N(\lambda), r^N_{well}(\lambda)\right], \tag{26}$$

where $\Delta H = H_s - H_l$, and P^{ex} and P^{ex}_{Gauss} are the excess pressure tensors due to the intermolecular potential and Gaussian well potential, respectively. The first term is due to pressure-volume work associated with deforming the box and the second term accounts for gradually turning on the Gaussian potential wells.

c. Stage c This is the final stage of the pseudo-supercritical transformation path. We now have a fluid constrained to solid configurationally phase space. The potential

energy function of this final stage as function of λ is

$$U_c(\lambda) = [\eta + (1-\eta)\lambda]\, U_{\text{int}\,er}(r^N) + (1-\lambda)\, U_{Gauss}\left(r^N, r^N_{well}\right) + \phi_{fw}. \quad (27)$$

And the derivative is given by

$$\frac{\partial U_c}{\partial \lambda} = (1-\eta)\, U_{\text{int}\,er}(r^N) - \mathrm{U}_{Gauss}\left(r^N, r^N_{well}\right). \quad (28)$$

4. Finding the temperature where ΔG is zero

The difference in excess Helmholtz free energy, ΔA^{ex}, between the crystalline and liquid phase at the approximate melting temperature is produced in the previous step by thermodynamic integration using three-stage pseudo-supercritical path. It is required to convert Helmholtz free energy to Gibbs free energy. This can be easily done into the difference in Gibbs free energy, ΔG through the simple relationship, $\Delta G = \Delta A^{ex} + \Delta A^{id} + PH\Delta(L_y L_x)$,where ΔA^{id} is the change in the ideal gas contribution to the Helmholtz free energy, P here is $P_{\text{xx}} = P_{\text{yy}}$. Additionally, the histogram reweighting analysis yields two free energy curves. The formulae used to compute Gibbs free energy difference with respect to a single state point is slightly modified from that in the original work.[52] For the liquid phase, $\{(\beta G)_{T_1,l} - (\beta G)_{T_i,l}\}$ is known and for the solid phase, $\{(\beta G)_{T_1,s} - (\beta G)_{T_i,s}\}$ is known, where the expression $(\beta G)_{Tm,n}$ indicates (βG) for the meta-stable phase n at state point T_{am}. Given that T_{am}, an approximate melting point, is the state point at which the thermodynamic integration is conducted, the following can be obtained:

$$[(\beta G)_{T_1,s} - (\beta G)_{T_{am},s}] + [\beta(G_{T_{am},s} - G_{T_{am},l})] - [(\beta G)_{T_i,l} - (\beta G)_{T_{am},l}] = [(\beta G)_{T_1,s} - (\beta G)_{T_i,l}]. \quad (29)$$

Equation (29) can be rearranged as

$$[(\beta G)_{T_1,s} - (\beta G)_{T_{am},s}] + [\beta(G_{T_{am},s} - G_{T_{am},l})] - [-(\beta G)_{T_1,l} + (\beta G)_{T_1,l} + (\beta G)_{T_i,l} - (\beta G)_{T_{am},l}] = [(\beta G)_{T_1,s} - (\beta G)_{T_i,l}], \quad (30)$$

which further can be simplified as

$$[(\beta G)_{T_1,s} - (\beta G)_{T_{am},s}] + [\beta(G_{T_{am},s} - G_{T_{am},l})] - [-\{(\beta G)_{T_1,l} - (\beta G)_{T_i,l}\} + \{(\beta G)_{T_1,l} - (\beta G)_{T_{am},l}\}] = [(\beta G)_{T_1,s} - (\beta G)_{T_i,l}], \quad (31)$$

where the first and third terms on the left side of Eq. (31) are obtained from the MHR analysis, while the second term comes from the pseudo-supercritical path by free energy calculation. The second term is yielded by combining relatively large free energy changes obtained over the transformation path.

III. SIMULATION DETAILS

In this work, two types of attractive pore walls are considered for the wall-fluid interaction viz., LJ 9-3 potential and Steele 10-4-3 potential. Gibbs free energy difference between solid and liquid phases is determined at a single state point as per the methodology described above. Thermodynamic melting temperature is evaluated where Gibb's free energy difference of two phases become zero.

First, we choose an approximate melting temperature, T_{am}, using hysteresis loop. This is done by performing two different types of $NP_{\text{xx}}(= P_{\text{yy}})HT$ simulation using LAMMPS[56] One for the quenching cycle and another for the heating cycle. The velocity-verlet algorithm is used to integrate the equation of motion with a time step, $\Delta t = 0.004$. The temperature and pressure are controlled using a Nosé–Hoover thermostat and barostat[57] with relaxation times of 2.0 and 5.0 for temperature and pressure, respectively. In the current work, the model fluid is confined between two structureless parallel slit surfaces separated by a distance H. H is varied from 5 to 20 molecular diameters. Approximately 4000–20 000 particles are used to run the simulations. Truncated and shifted potential is used with a cutoff radius of 5σ for both the particle-particle and wall-fluid interaction throughout this work. The periodic boundary condition is applied in only two directions, i.e., x and y. Pressure along the periodic dimensions are kept fixed: $P_{xx} = P_{yy} = 1$. In case of quenching, the initial liquid configurations are taken randomly at a temperature $T = 1.2$. Cooling is performed in a step-by-step procedure after each 2.5×10^6 MD time-steps; T is gradually reduced in steps of 0.03 from 1.2 to 0.3. During the heating process, we have taken the last configuration of the quenching process as the initial configuration. Heating is also performed using a step-by-step procedure. After 2.5×10^6 MD time-steps, T is progressively increased by 0.03, and heating is continued until the solid has completely lost its crystallinity. During both quenching and heating cycles, the density is recorded as a function of temperature.

To construct the Gibbs free energy curves of the crystalline and liquid phases under confinement, using MHR, histograms are collected from $NP_{\text{xx}}(= P_{\text{yy}})HT$ molecular dynamics simulations using the Nose´-Hoover thermostat-barostat algorithm[57] with anisotropic cell fluctuations. We perform 11 simulations for each phase. The temperature is chosen according to the following relationship:

$$T_i = T_{am} + \sum_{n=-5}^{5} n\Delta T,$$

where T_{am} is the approximate melting temperature estimated from the hysteresis data; $\Delta T = 0.0205$ is chosen according to Eike *et al.*[52]

The initial configurations for solid-phase or liquid phase simulations are taken from the NPT simulation run used for hysteresis analysis. Following sufficient equilibration, for around 200 ps, simulations are conducted for 10 ns using a time step of 4 fs. The solid phase simulations are conducted by progressively increasing the temperature by $\Delta T = 0.0205$, while liquid phase temperature is gradually decreasing by the same order. The reference state points are chosen along the quenching and heating paths, for liquid and solid phases respectively, at the lowest temperature, $T_i = T_{am} - 5\Delta T$. The system's potential energy U and volume V are recorded at every time step, and these data are converted into histograms.

The step c calculates the Gibbs free energy difference at T_{am} using three-stage thermodynamic integration method. Simulations at each stage are conducted under NVT ensemble. For each integration stage, ten simulations were conducted, with the values of λ chosen according to the standard ten point Gauss-Legendre integration scheme. For the Gaussian potential well parameters, values are calculated as per Grochola.[44] The value of the scaling parameter is kept fixed at $\eta = 0.1$.[52]

Simulations for the first stage of the transformation path are started from a random initial configuration (i.e., $\lambda = 0$) which is obtained during hysteresis runs. Subsequently for each λ initial configuration is taken from its previous λ simulation. For all the three stages time step is fixed at 0.004, and total simulation run for each λ is 5×10^6. For the second stage, stage b, we take the last configuration of the stage-a as the initial configuration. However, to obtain the final configuration we put dummy atoms on the crystal lattice obtained from the heating run. In order to assess the error for this stage we have considered 3–4 initial crystal configurations (obtained from the hysteresis runs). The Gaussian potential wells are attached to these dummy atoms. Box dimensions (L_X, L_Y) are modified according to λ values as derived in Sec. II B. The initial configuration for the third stage is taken from the heating run of hysteresis loop at T_{am} and the dummy atoms are created as described for the second stage. Thermodynamic integration is solved with the help the standard ten point Gauss-Legendre integration scheme for all the stages.

We separately performed simulations as per Eike *et al.*[52] to determine the thermodynamic melting temperature of the bulk LJ fluid using the three-stage pseudo-critical transformation path along with MHR.

IV. RESULTS AND DISCUSSION

A. LJ 9-3 surface

We start our discussion with the strongly attractive LJ 9-3 wall case, with relative wall-fluid strength $\alpha = 2.32$. Pore width is varied from 20 to 5 molecular diameters. Figure 2 presents the density along the pore width for the quenching path (similar is the case for the heating path). At higher temperatures (see for example $T = 1.2$), density peak of the layers are not pronounced. As the temperature decreases the peak height increases, and sharp distinct peaks are observed for the solid phase. From the change in the peak height and shape, solid and liquid phases can be distinguished and an approximate melting temperature can be estimated. However, determination of the true thermodynamics melting transition point requires calculation of the free-energy for both the solid and liquid phases.

As stated earlier, the first step of evaluating the true thermodynamic melting temperature is to determine an approximate melting temperature which is done using hysteresis loop along the phase transition. We first calculate the overall density of the confined system along the quenching and heating paths. Fig. 3 shows a plot of the density as a function of the temperature for both cases, for $H = 8$. As the liquid is quenched, the density gradually increases and at a certain temperature the density rises drastically. In case of heating, the density decreases and at a particular temperature the density drops sharply. The hysteresis loop, as shown in Fig. 3, indicates a first-order phase-transition. A wide meta-stable region is observed around the true phase-transition point. The melting point is adjacent to this meta-stable region. It clearly shows that abrupt density change or a discontinuous drop in density occurs at $T = 0.87$, which indicates that the true thermodynamic melting temperature would be lower than this temperature. In Fig. 3 vertical dash line represents the approximate melting temperature $T_{am} = 0.72$, at which free energy difference is evaluated using pseudo-supercritical transformation path. Solid and liquid box lengths are determined from the corresponding densities as shown by horizontal dotted lines.

Gibbs free energy curves are constructed taking $T = 0.72$ as an intermediate point. Simulations are performed at 11

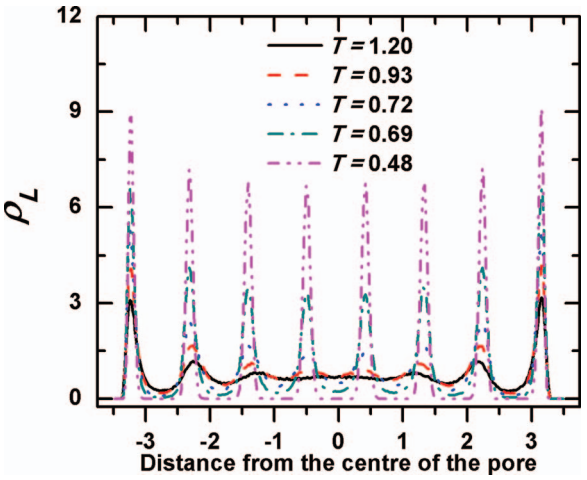

FIG. 2. Local density (ρ_L) as a function of pore distance for $H = 8.0$, for the quenching case.

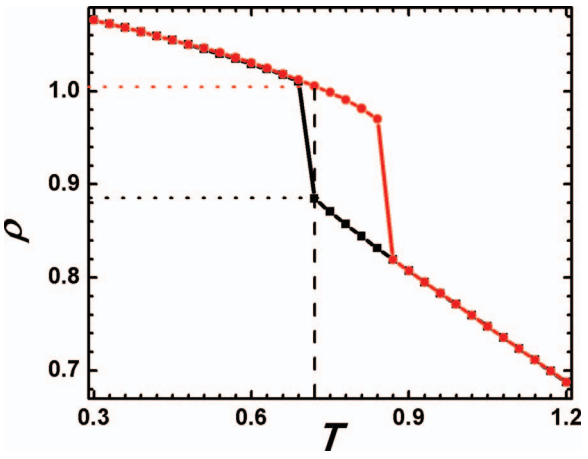

FIG. 3. Density as a function of temperature for solid and liquid phases at $P_{xx} = P_{yy} = 1.0$ for pore width, $H = 8$, for $\varepsilon_{wf} = 0.4348$ and $\alpha = 2.32$. Symbols square and circle represent quenching and heating cycles, respectively. The solid (top curve) progressively heated from $T = 0.3$ to 1.2, while the liquid (bottom curve) is quenched progressively from $T = 1.2$ to 0.3. Vertical dotted line indicates an approximate melting temperature (T_{am}). Horizontal dotted lines indicate corresponding densities of the solid and liquid phases at T_{am}.

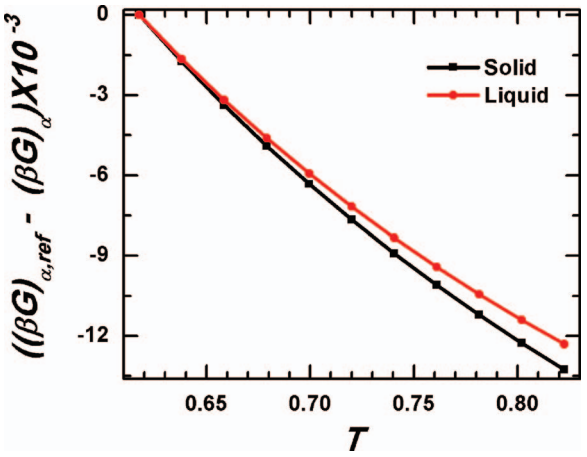

FIG. 4. Relative Gibbs free energy curves as a function of temperature for confined Lennard-Jones system for $H = 8$ relative to their respective reference states, constructed from MHR.

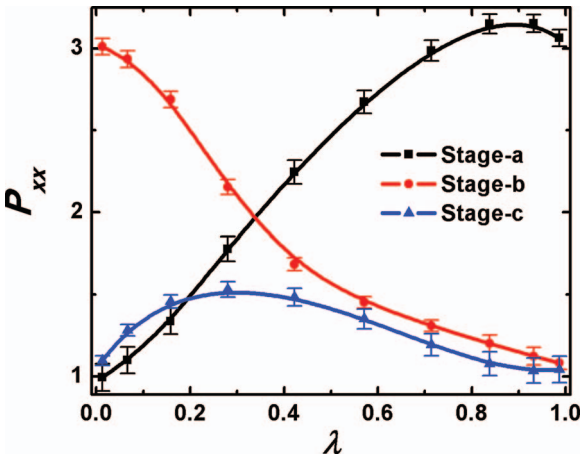

FIG. 5. P_{xx} as a function of λ for three steps for $H = 8$. Pressures at the beginning of stage-a and pressure at the end of stage-c are same, which is the essential characteristic for the three-stage pseudo-supercritical transformation path. P_{yy}'s behavior is also similar in nature.

different temperatures, as described earlier, taking approximate melting temperature as an intermediate middle/central point of 11 simulations. For each temperature, two sets of simulations are performed one for the heating case and another for the quenching case, resulting in 22 histograms.

The relative Gibbs free energy curves for both the phases are generated by collecting the histograms separately for solid and liquid phases. For each branch, Eqs. (14) and (15) are solved iteratively by assuming initial guess values to determine the weights C_i^Z. Subsequently these weights are used in Eq. (18) to construct the full Gibbs free energy curves with respect to the lowest temperature state point for each phase. Fig. 4 presents the Gibbs free energy curves for the solid and liquid phases with respect to their respective reference state. The next step is evaluation of Gibbs free energy difference between two phases at an approximate melting temperature. Change in Gibbs free energy can be expressed as

$$\Delta G = \Delta G_{\mathrm{a}} + \Delta G_{\mathrm{b}} + \Delta G_{\mathrm{c}} = \Delta A^{ex} + \Delta A^{id} + PH\Delta(L_x L_y). \tag{32}$$

The term ΔA^{ex} is produced from the three-stage pseudo-supercritical transformation path method, ΔA^{id} is the change in the ideal gas contribution to the Helmholtz free energy, and the last term is the pressure volume (pressure here corresponds to the lateral components of the pressure tensor, i.e., $P = P_{xx} = P_{yy}$) work due to the change in volume from liquid to solid.

Thermodynamic integration is conducted at an approximate melting temperature along the pseudo-supercritical path, through which solid and liquid phases are connected avoiding the first order phase transition. The box lengths for solid and liquid phases are determined from their respective densities as shown in Fig. 3. The box lengths are chosen such a way that $P_{xx} = P_{yy} = 1$ remain constant at the beginning of the stage-a and at the end of the stage-c which is shown in Fig. 5. We also observed overall pressure to remain constant. Plots of $\langle \partial U / \partial \lambda \rangle_{NVT\lambda}$ as function of λ for three stages of thermodynamic integration are shown in Fig. 6, which shows that curves are continuous and integrable for all the three steps. Further, we have also checked the reversibility of the thermodynamic path considered in this work. For all the three cases, error bars are of the order of symbol size. The different contributions to the Gibbs free energy for all the wall separations are shown in Table I.

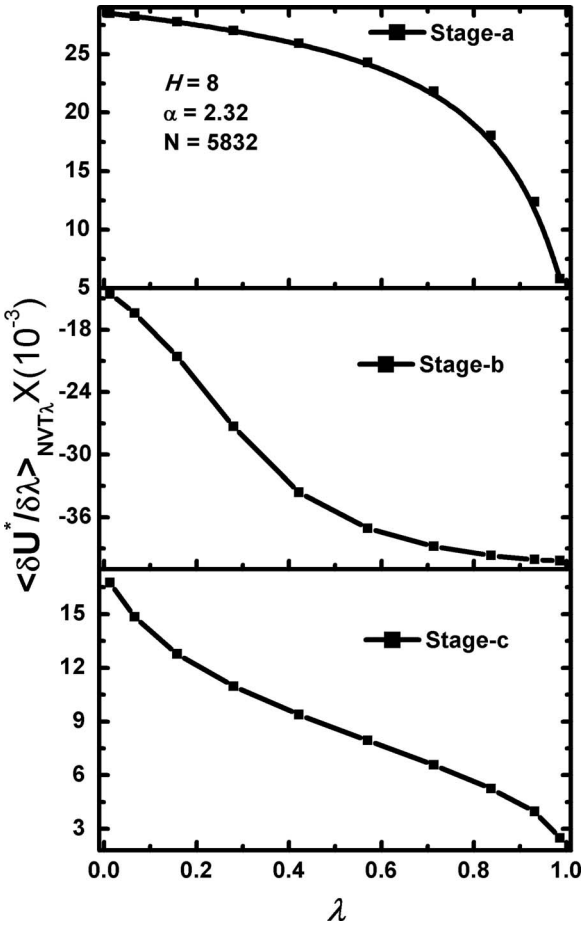

FIG. 6. $\langle \partial U / \partial \lambda \rangle_{NVT\lambda}$ as a function of λ for three-stage pseudo-supercritical transformation path for the confined Lennard-Jones system for $H = 8$.

TABLE I. Estimated true thermodynamic melting temperature, T_m, and various contributions to the Gibbs free energy, for different pore sizes, H, with variable wall-fluid interaction strength at approximate melting temperature (T_{am}). ΔG denotes Gibbs free energy difference at T_{am}. ρ_L and ρ_S represent corresponding densities of liquid and solid respectively at T_{am}.

H	T_{am}	ρ_L	ρ_S	ΔA^{ex}	ΔA^{id}	$P\Delta V$	ΔG	T_m
				Wall(LJ 9-3) $\varepsilon_{wf} = 0.4348$, $\alpha = 2.32$				
20.0	0.75	0.869	0.966	-50.327 ± 0.231	1462.454	-2130.132	-717.915	0.767 ± 0.001
16.0	0.72	0.912	0.943	-79.981 ± 0.765	461.452	-545.097	-163.625	0.773 ± 0.001
12.0	0.78	0.864	0.961	354.179 ± 0.973	863.154	-1215.040	2.294	0.782 ± 0.001
8.0	0.72	0.885	1.005	-77.663 ± 1.574	537.906	-792.706	-332.463	0.813 ± 0.002
7.5	0.75	0.868	0.949	-31.595 ± 0.635	382.820	-562.557	-211.333	0.782 ± 0.002
7.0	0.72	0.893	1.007	-42.561 ± 0.848	484.360	-709.683	-267.884	0.775 ± 0.002
6.5	0.75	0.872	0.950	-32.985 ± 0.689	359.334	-526.495	-200.146	0.823 ± 0.002
6.0	0.72	0.874	0.972	-44.936 ± 0.942	368.823	-556.085	-232.198	0.763 ± 0.002
5.5	0.78	0.836	0.915	-22.994 ± 0.526	339.593	-497.963	-181.364	0.814 ± 0.004
5.0	0.75	0.812	0.899	-17.693 ± 0.434	307.741	-480.745	-190.697	0.783 ± 0.003
				Wall(Steele 10-4-3) $\varepsilon_{wf} = 0.3325$, $\alpha = 1.65$				
7.5	0.75	0.871	0.972	-50.414 ± 0.994	480.800	-697.377	-266.99	0.823 ± 0.006
				Wall(Steele 10-4-3) $\varepsilon_{wf} = 0.4348$, $\alpha = 2.14$				
7.5	0.78	0.855	0.973	-194.199 ± 4.040	581.367	-817.417	-430.249	0.854 ± 0.005

Once the Gibbs free energy difference of two phases is determined at an approximate melting temperature, it is no longer difficult to convert liquid Gibbs free energy curve relative to a solid reference state using Eq. (31). The two Gibbs free energy curves with respect to a single reference state point are shown in the Fig. 7. Using the relative free energy between the crystalline and liquid phases at a single point, the free energy difference between crystalline and liquid phases can be evaluated for all other points. By determining ΔG in this way over a range of temperatures, a ΔG vs. temperature curve can be produced, and the temperature where this curve is zero produces a single coexistence point or thermodynamic melting temperature The Gibbs free energy difference, ΔG, between solid-liquid phases as a function of temperature is shown in Fig. 8, which clearly shows the temperature at which equality in free energy of both the solid and liquid phases occur. The coexistence temperature calculated using the above mentioned method for $H = 8$ is 0.813 which is well agreement with our earlier results based on heuristic method.[20] However, this is not the case for all other different slit separations. Different contribution to the Gibbs free energy and estimated true thermodynamic melting temperatures for different slit separations are given in Table I. We have also evaluated the melting temperature of bulk LJ system using the three-stage pseudo-critical transformation path along with MHR. Our calculated value 0.763 is consistent with that of Eike *et al.*[52] We observed an elevation of melting temperature under confinement as studied in this work. This agrees with the results of Radhakrishnan and co-workers[21] based on Landau theory and orientational order parameter formulation, which predicts that melting temperature should elevate for $\alpha > 1.15$. However, there is no certain relation between the melting temperature and the slit separation, and is oscillatory in nature as also found by earlier worker via different methods.[21,41,42] Wan *et al.*[41] evaluated the order-disorder transition temperature, based on visual inspection and 2D order parameter. Though they did not

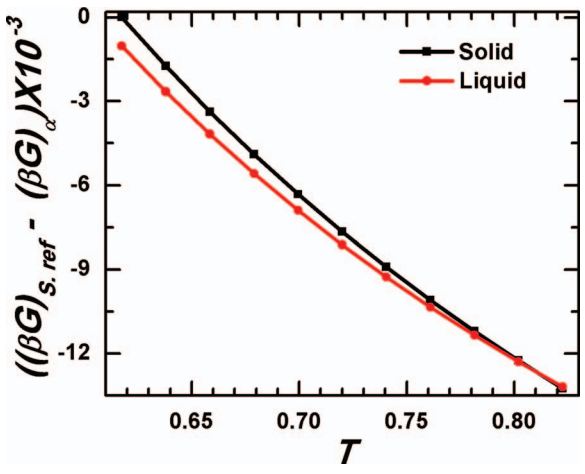

FIG. 7. Relative Gibbs free energy as a function temperature for $H = 8$ constructed from MHR. Both branches are relative to the solid reference state.

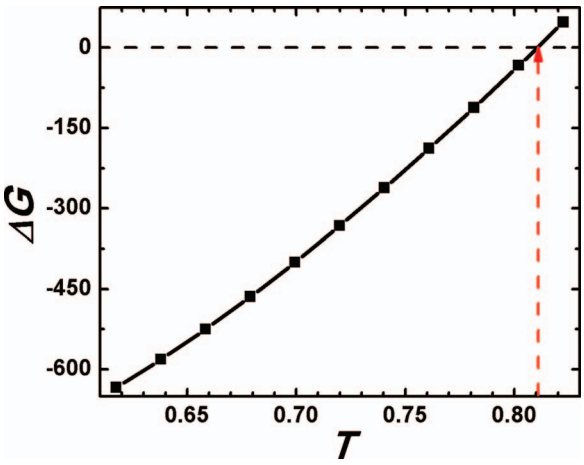

FIG. 8. ΔG as a function of T for $H = 8$. Vertical arrow dashed line indicates solid-liquid coexistence temperature or true thermodynamic melting temperature (T_m), where Gibbs free energy difference, ΔG, between the solid and the liquid phases is zero.

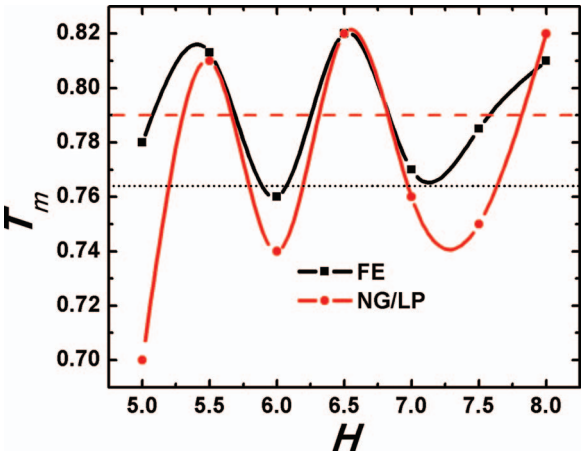

FIG. 9. Comparison of thermodynamic melting temperature with kinetic melting temperature for different pore sizes. Horizontal dotted line (bottom line), black in color, represents the bulk kinetic melting temperature. Horizontal dotted line in red color (top line) represents the bulk thermodynamic melting temperature.

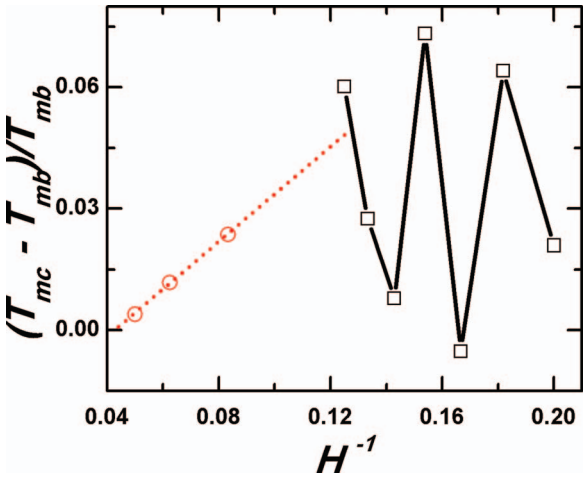

FIG. 10. The shift in melting temperature reduced by the bulk melting temperature, T_m $[(T_{mc} - T_{mb})/T_{mb}]$, as a function of inverse of the pore size, H. T_{mb} is the bulk melting temperature and T_{mc} is the melting temperature under confinement. The dashed line is a fit to the data of $H = 12$, 16, and 20, based on the Gibbs Thomson equation. The firm lines connect square symbols corresponding to $H = 5$–8 molecular diameter, with an increment of 0.5.

report the direct coexistence solid-liquid temperature under confinement, free energy of nano-confined solids using Einstein method revealed similar oscillatory behavior. Kaneko and co-workers[42] determined the melting/freezing temperature from the discontinuities of potential energy and density. It should be noted that slit pore sizes in the studies of Wan *et al.*[41] and Kaneko and co-workers[42] were in the range of 2–7 molecular diameters. As we later show that beyond $H = 12$, we observed suppression in the oscillatory behavior.

Fig. 9 shows the thermodynamic melting temperature, with respect to the bulk value, for pore sizes $H = 5$–8. Fig. 9 also presents a comparison of the kinetic melting temperature,[20] based on Lindemann parameter and Non-Gaussian parameter, with the thermodynamic melting temperature. In our earlier work,[20] we have reported that the kinetic melting temperature displays both elevation and depression behavior with wall separation. Interestingly, in this work we observe only an elevation in the thermodynamical melting temperature compare to that of bulk solid. However, oscillatory behavior in the melting temperature (kinetic or thermodynamic) is a generic behavior with pore size as studied in this work. The oscillation in melting temperature indicates incommensurability of the crystal structures with the space available in the pores. However, at larger pore sizes melting temperature is closer to the bulk value, which indicate that confinement effect gradually diminish as pore size increases. The shift in melting temperature for H $\geq$ 12 is in linear relationship with inverse of the pore size and obeys the Gibbs-Thomson equation, as shown in Fig. 10. Based on the data of H = 12, 16, and 20, we expect the confinement effect to be insignificantly for the pore size >25. This observation is in line with that observed for the vapor-liquid coexistence under confinement.[58]

It should be noted that the structure observed just before melting for both the heuristic and thermodynamics based methods are indifferent, which may be the reason for similarly in the overall behavior of melting temperature against pore size using kinetic and thermodynamic approaches. The qualitative agreement between thermodynamic and kinetic approaches supports the usage of heuristic methods such as non-Gaussian and Lindemann parameter (for qualitative prediction), which is straight forward and computationally extremely less intensive.

B. Steele 10-4-3 surface

We now turn our attention to a different wall-fluid interaction, i.e., 10-4-3 Steele potential. In this case we perform simulation for $H = 7.5$ with two sets of relative wall-fluid interaction $\alpha = 1.64$ and 2.14. The approximate melting temperature is determined by computing density as a function of temperature, as per the details mentioned in Sec. IV A. Based on the sudden change in density at $T = 0.87$ for $\alpha = 2.14$, we consider $T = 0.78$ as an approximate melting temperature. The construction of Gibbs free energy curves is done in a temperature range from 0.6775 to 0.8825 with a temperature increment of $\Delta T = 0.0205$. Total 22 histograms, 11 for each phase, are collected. After reweighting all the histograms, two Gibbs free energy curves are constructed with respect to their respective reference states.

The Gibbs free energy difference is evaluated at the approximate melting temperature from three stage pseudo-supercritical transformation path. The box lengths of solid and liquid phases are selected based on their respective densities such that the $P_{xx} = P_{yy} = 1$ at the beginning of the transformation path and end of the transformation remain constant. Plots of pressure versus λ are similar to that seen in Fig. 5 for three stages. Plots of $\langle \partial U / \partial \lambda \rangle_{NVT\lambda}$ as a function of λ are smooth and integrable as presented in Fig. 6. The different contributions to the Gibbs free energy difference at the approximate melting temperature are shown in Table I.

Using the Gibbs free energy difference from thermodynamic integration and with the help of Eq. (31) the liquid free energy curve is transferred to the same reference as the

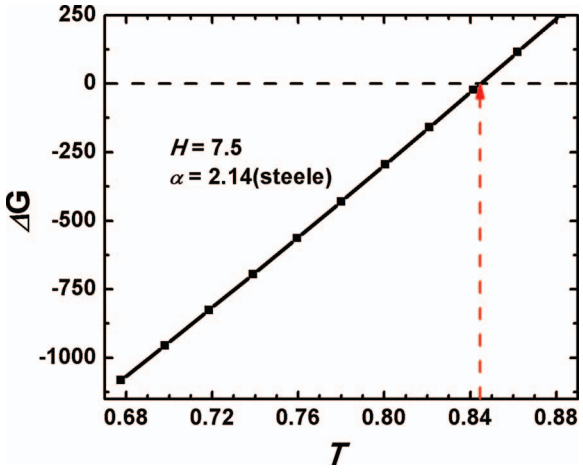

FIG. 11. ΔG as a function of T for $H = 7.5$. Horizontal dashed line represents ΔG = 0, and vertical arrow dashed line indicates solid-liquid coexistence temperature or true thermodynamic melting temperature(T_m) of solid where Gibbs free energy difference between solid and liquid is zero.

solid free energy curve. The Gibbs free energy curves are constructed after shifting to the same reference state. A plot of ΔG as function of temperature is presented in Fig. 11. The computed coexistence temperature or melting temperature is $T = 0.855$. This value is slightly higher than the value of $T = 0.83$ as reported by Radhakrishnan *et al.*[21] The melting temperature for relative wall-fluid interaction $\alpha = 1.64$ is $T = 0.823$ where Radhakrishnan and co-workers[21] reported 0.810. Though the values are in close proximity with the literature value, it should be noted that the thermodynamics melting temperature evaluated in this work corresponds to the temperature at which solid and liquid phases are in equilibrium under confinement. This is in contrast to the system studied by Radhakrishnan and co-workers, where they considered the temperature corresponding to the confined solid-bulk liquid coexistence. Hence, the results are expected to be slightly different. This work though presents the results of simple LJ system yet it can be extended/implemented to confined complex molecular systems, which we plan to undertake in our future work.

C. Crystal structures in confined slit pore

We also rigorously studied the structure of confined crystal for all wall separations, for earlier mentioned wall-fluid interaction. We estimate in-plane order parameter: $\psi_k = \left\langle \frac{1}{N_b} \left| \sum_{j=1}^{N_b} \exp\left(ik\theta_j\right) \right| \right\rangle$, where $k = 4$ and 6 represents square and triangular symmetry, respectively; N_b is the total number of near neighbors at a distance of 1.5 in each layer and θ_j is the angle formed by a particle with its nearest-neighbor atom. $\Psi_k = 1$ indicates that there is complete k-time symmetry in the crystal structure or in the layer and $\Psi_k = 0$ means there is no k-time symmetry in the layer. A high value of Ψ_4 indicates square dominated structure in the plane and that for Ψ_6 indicates triangular symmetry. We observe Ψ_6 values are always higher than Ψ_4 for all the wall separations, except for $H = 5$.

Table II summarizes the crystal structure and orientation order parameter for various wall separations. All structures

TABLE II. Representation of the change in crystal structure and orientation order parameter with wall separation.

H	Structures	Ψ_4	Ψ_6
5.0	5S	0.503	0.044
5.5	5T	0.133	0.610
6.0	6T	0.117	0.768
6.5	6T	0.145	0.710
7.0	7T	0.159	0.549
7.5	7T	0.104	0.779
8.0	8T	0.034	0.745

are taken at $T = 0.7$. Though we present only the results for the contact layer, the nature of all the layers is similar. Here, nS represents n-layered solid of square-like symmetry in each layer, which basically are FCC(100) planes; and nT represents n-layered solid of triangular or hexagonal-like symmetry in each layer, which mainly are FCC(110) or FCC(111) plane of orientation. Fig. 12 presents the side views and top

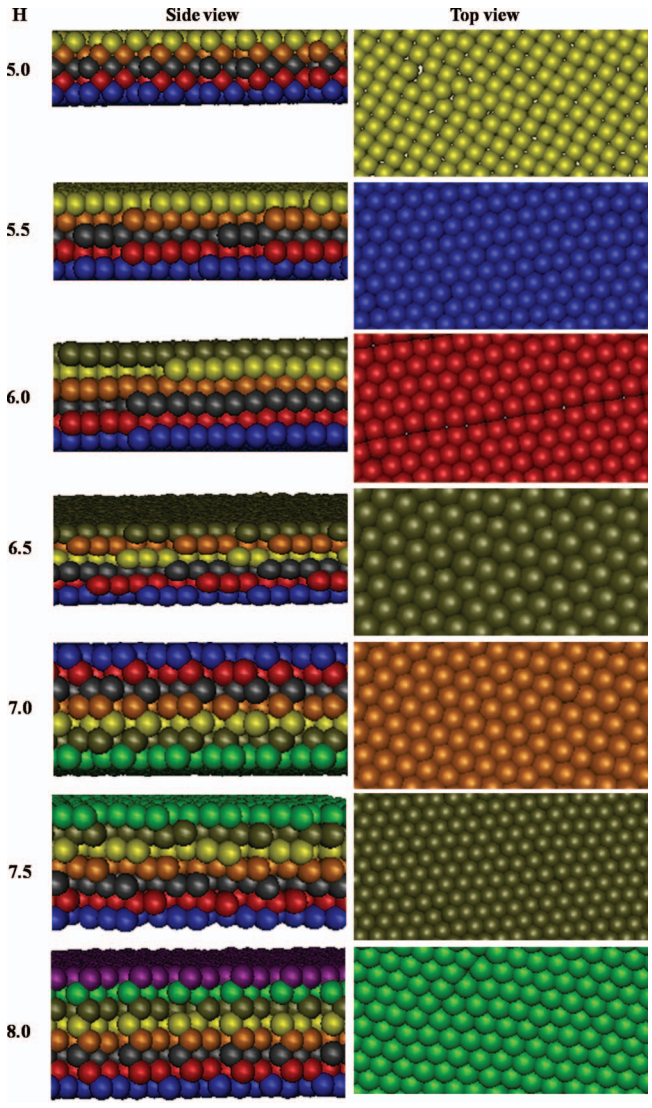

FIG. 12. Representative snapshots (side and top views) for LJ particles confined in parallel slit pores.

views of the crystal structures, for different wall separation. For example, at $H = 5$ it is FCC 100 plane however it is not perfect and some distortion from the square lattice is clearly visible in the top view. On the other hand, at $H = 6.5$, a highly ordered FCC 111 plane is observed, as also supported by the order parameter value (see Table II). However in case of $H = 6$ both the square and triangular symmetries are observed. At higher H, hexatic phase is dominant. The observed structures are in agreement with that seen in earlier reports.[42,59]

V. CONCLUSION

In this work, we present the melting behavior of LJ solids confined in strongly attractive slit pores of different pore sizes. Thermodynamic melting temperatures of confined LJ fluids are evaluated using a pseudo-supercritical transformation path connecting the solid and liquid phases without first order phase transition along with multiple histogram reweighting. The thermodynamic melting temperature for almost all wall separations is higher than the bulk case, which is contrary to the behavior seen for the kinetic melting temperature. Oscillatory nature of melting temperature for pore size, H $\leq$ 8, is confirmed with an accurate estimate of true melting temperature. On the other hand, for $H \geq 12$ the thermodynamic melting temperature is in linear relationship with inverse of the pore size, as predicted by the Gibbs-Thomson equation. The method employed is advantageous over other existing methods, since separate evaluation of free energy of each phase is not required. Hence, no need to find out appropriate reference states with known free energy values. The method is extremely useful to locate a single coexistence point, which could be used as an initial guess for generating full phase diagram.

The method used in this work utilizes the overall behavior of confined crystals; hence, cannot identify melting temperature of confined layers. Further, it requires large number of simulations in series, which is computationally costly. However, it can be made efficient by the use of replica exchange molecular dynamics. We observed kinetic melting temperature based on heuristic methods behaves similar to that of thermodynamic temperature with the pore size. Considering similarities, non-Gaussian and Lindemann methods are promising as these methods can be used to provide qualitative nature of melting temperature of confined solids relatively quickly.

ACKNOWLEDGMENTS

This work was supported by the Department of Science and Technology, Government of India.

[1]Z. Zhang, D. Gekhtman, M. S. Dresselhaus, and J. Y. Ying, Chem. Mater. **11**, 1659 (1999).
[2]M. Alcoutlabi and G. B. McKenna, J. Phys.: Condens. Matter **17**, R461 (2005).
[3]J. A. Duffy, N. J. Wilkinson, H. M. Fretwell, and M. A. Alam, J. Phys.: Condens. Matter **7**, L27 (1995).
[4]K. M. Unruh, T. E. Huber, and C. A. Huber, Phys. Rev. B **48**(12), 9021 (1993).
[5]J. Klein and E. Kumacheva, Science **269**, 816 (1995).
[6]L. D. Gelb, K. E. Gubbins, R. Radhakrishnan, and M. Sliwinska-Bartkowiak, Rep. Prog. Phys. **62**, 1573 (1999).
[7]C. Alba-Simionesco, B. Coasne, G. Dosseh, G. Dudziak, K. E. Gubbins, R. Radhakrishnan, and M. Sliwinska-Bartkowiak, J. Phys.: Condens. Matter **18**, R15 (2006).
[8]J. Warnock, D. D. Awschalom, and M. W. Shafer, Phys. Rev. Lett. **57**(14), 1753 (1986).
[9]C. A. Murray and D. H. V. Winkle, Phys. Rev. Lett. **58**(12), 1200 (1987).
[10]Y. Tang, A. J. Armstrong, R. C. Mockler, and W. J. O. Sullivan, Phys. Rev. Lett. **62**(20), 2401 (1989).
[11]C. A. Murray, W. O. Sprenger, and R. A. Wenk, Phys. Rev. B **42**(1), 688 (1990).
[12]C. A. Murray, W. O. Sprenger, and R. A. Wenk, J. Phys.: Condens. Matter **2**, SA385 (1990).
[13]P. T. Cummings, H. Docherty, C. R. Iacovella, and J. K. Singh, AIChE J. **56**(4), 842 (2010).
[14]H. Dominguez, M. P. Allen, and R. Evans, Mol. Phys. **96**(2), 209 (1999).
[15]H. C. Huang, S. K. Kwak, and J. K. Singh, J. Chem. Phys. **130**, 164511 (2009).
[16]M. Schmidt and H. Löwen, Phys. Rev. Lett. **76**(24), 4552 (1996).
[17]M. Miyahara and K. E. Gubbins, J. Chem. Phys. **106**, 2865 (1997).
[18]M. W. Maddox and K. E. Gubbins, J. Chem. Phys. **107**(22), 9659 (1997).
[19]W. J. Ma, J. R. Banavar, and J. Koplik, J. Chem. Phys. **97**(1), 485 (1992).
[20]C. K. Das and J. K. Singh, Theor. Chem. Acc. **132**, 1351 (2013).
[21]R. Radhakrishnan, K. E. Gubbins, and M. Sliwinska-Bartkowiak, J. Chem. Phys. **112**(24), 11048 (2000).
[22]M. Sliwinska-Bartkowiak, G. Dudziak, R. Sikorski, R. Gras, R. Radhakrishnan, and K. E. Gubbins, J. Chem. Phys. **114**(2), 950 (2001).
[23]R. Radhakrishnan, K. E. Gubbins, and M. Sliwinska-Bartkowiak, J. Chem. Phys. **116**(3), 1147 (2002).
[24]R. Radhakrishnan and K. E. Gubbins, Mol. Phys. **96**, 1249 (1999).
[25]B. Coasne, J. Czwartos, K. E. Gubbins, F. R. Hung, and M. Sliwinska-Bartkowiak, Adsorption **11**, 301 (2005).
[26]Z. H. Jin, P. Gumbsch, K. Lu, and E. Ma, Phys. Rev. Lett. **87**(5), 055703 (2001).
[27]A. V. Granato, D. M. Joncich, and V. A. Khonik, Appl. Phys. Lett. **97**, 171911 (2010).
[28]M. Born, J. Chem. Phys. **7**, 591 (1939).
[29]F. Delogu, J. Phys.: Condens. Matter **18**(24), 5639 (2006).
[30]J. P. Hansen and L. Verlet, Phys. Rev. **184**(1), 151 (1969).
[31]W. Gotze and M. Liicke, J. Low Temp. Phys. **25**(5/6), 671 (1976).
[32]J. Q. Broughton, G. H. Gilmer, and J. D. Weeks, Phys. Rev. B **25**(7), 4651 (1982).
[33]S. Ranganathan and K. N. Pathak, Phys. Rev. A **45**(8), 5789 (1992).
[34]R. Radhakrishnan and K. E. Gubbins, J. Chem. Phys. **111**(19), 9058 (1999).
[35]J. R. Errington, J. Chem. Phys. **120**, 3130 (2004).
[36]M. B. Sweatman and N. Quirke, Mol. Simul. **30**, 23 (2004).
[37]M. B. Sweatman, Phys. Rev. E **72**, 016711 (2005).
[38]M. B. Sweatman, A. A. Atamas, and J.-M. Leyssale, J. Chem. Phys. **128**, 064102 (2008).
[39]M. Mehta and D. A. Kofke, Mol. Phys. **79**, 39 (1993).
[40]D. A. Kofke, J. Chem. Phys. **98**, 4149 (1993).
[41]L. Wan, C. R. Iacovella, T. D. Nguyen, H. Docherty, and P. T. Cummings, Phys. Rev. B **86**, 214105 (2012).
[42]T. Kaneko, T. Mima, and K. Yasuoka, Chem. Phys. Lett. **490**, 165 (2010).
[43]K. Koga and H. Tanaka, J. Chem. Phys. **122**(10), 104711 (2005).
[44]G. Grochola, J. Chem. Phys. **120**(5), 2122 (2004).
[45]W. A. Steele, Surf. Sci. **36**, 317 (1973).
[46]P. A. Monson and D. A. Kofke, Adv. Chem. Phys. **115**, 113 (2000).
[47]J. R. Morris, C. Z. Wang, K. M. Ho, and C. T. Chan, Phys. Rev. B **49**(5), 3109 (1994).
[48]A. M. Ferrenberg and R. H. Swendsen, Phys. Rev. Lett. **61**, 2635 (1988).
[49]A. M. Ferrenberg and R. H. Swendsen, Phys. Rev. Lett. **63**, 1195 (1989).
[50]J. Chang and S. I. Sandler, J. Chem. Phys. **118**(18), 8390 (2003).
[51]J. Chang, A. M. Lenhoff, and S. I. Sandler, J. Chem. Phys. **120**(6), 3003 (2004).
[52]D. M. Eike, J. F. Brennecke, and E. J. Maginn, J. Chem. Phys. **122**, 014115 (2005).

[53]K. Kiyohara, K. E. Gubbins, and A. Z. Panagiotopoulos, J. Phys. Chem. **106**(8), 3338 (1997).
[54]P. B. Conrad and J. J. d. Pablo, Fluid Phase Equilib. **150–151**, 51 (1998).
[55]N. Karasawa and W. A. Goddard III, J. Phys. Chem. **93**, 7320 (1989).
[56]S. J. Plimpton, J. Comput. Phys. **117**, 1 (1995).
[57]G. J. Martyna, M. E. Tuckerman, D. J. Tobias, and M. L. Klein, Mol. Phys. **87**, 1117 (1996).
[58]S. K. Singh, A. K. Saha, and J. K. Singh, J. Phys. Chem. B **114**, 4283 (2010).
[59]T. Kaneko, K. Yasuoka, and X. C. Zeng, Mol. Simul. **38**(5), 373 (2012).